SUPPLEMENTARY INFORMATION

doi:10.1038/nature16530

Table of Contents

General Considerations

Depleted uranium (DU) typically consists of +99.7% ^{238}U, a weak α-emitter with a half-life of 4.47 • 10^9 years. The radiologic toxicity of DU is about a million times smaller than the chemical toxicity and hence should be treated with the same safety precautions as other heavy metals, which are also considered carcinogenic [1].

Spectroscopic Details

^{1}H NMR Spectroscopy

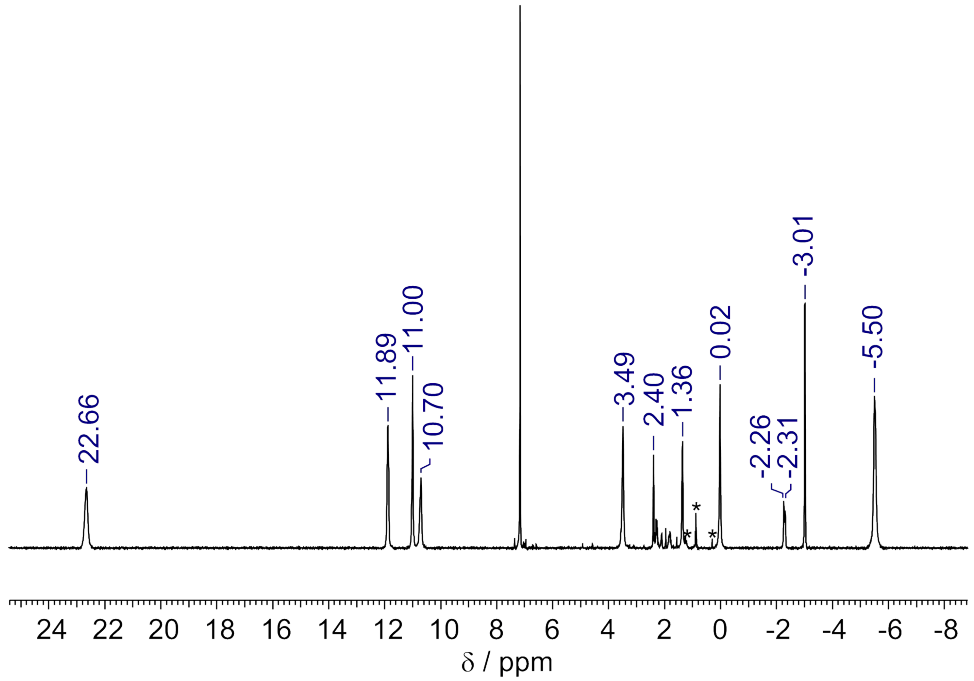

Fig. S1 | ^{1}H NMR of [[(^{Ad,Me}ArO)$_3$mes)U(OH)(THF)] **2–OH** recorded in C_6D_6, impurities (*n*-pentane and silicon grease) are marked with an asterisk.

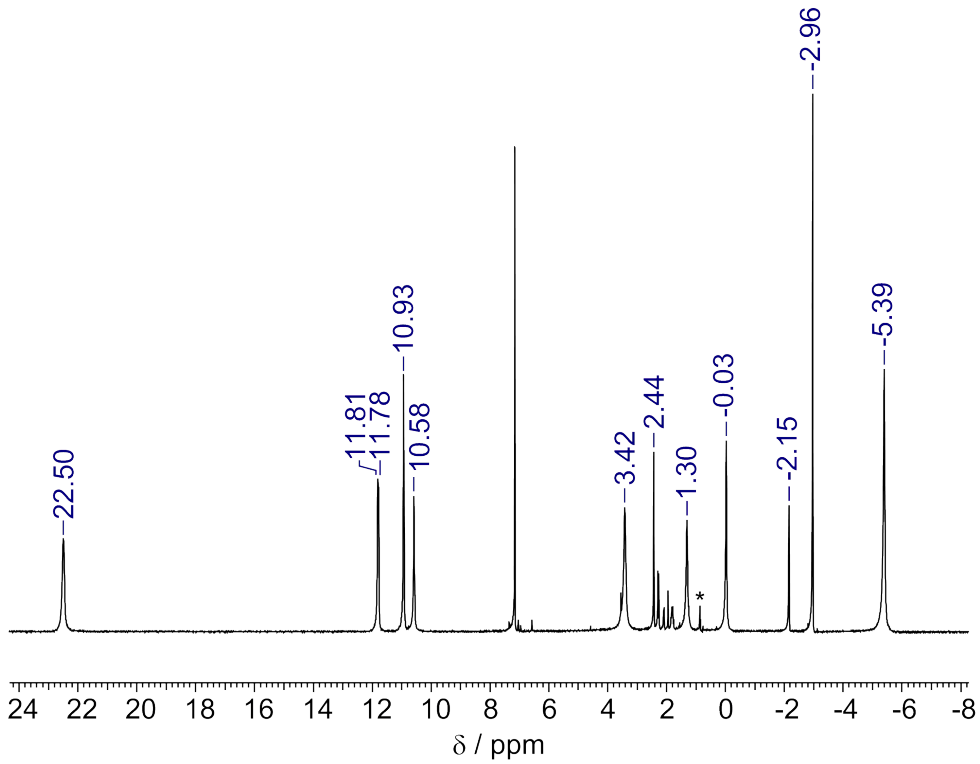

Fig. S2 | ^{1}H NMR of [[(^{Ad,Me}ArO)$_3$mes)U(OD)(THF)] **2–OD** recorded in C_6D_6, n-pentane is marked with an asterisk.

In addition to the mechanistic study presented in the maintext of the manuscript, a scrambling experiment was performed, where a 1:1 mixture of H_2O and D_2O in THF was electrolyzed by catalyst **1**.

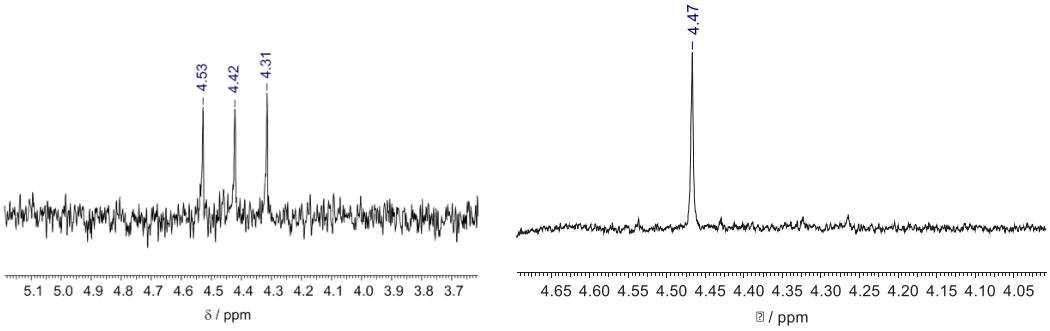

Fig. S3 | ^{1}H NMR spectra in C_6D_6 of an HD reference sample (*left*) and a sample of the headspace of a bulk electrolysis experiment, including 10 mL of THF, with 10 mg of catalyst, 20 µL of H_2O, and 20 µL of D_2O, clearly showing H_2 (at δ = 4.47) and possibly traces of HD (*right*) that remain questionable after 16.000 scans (40-hr-experiment).

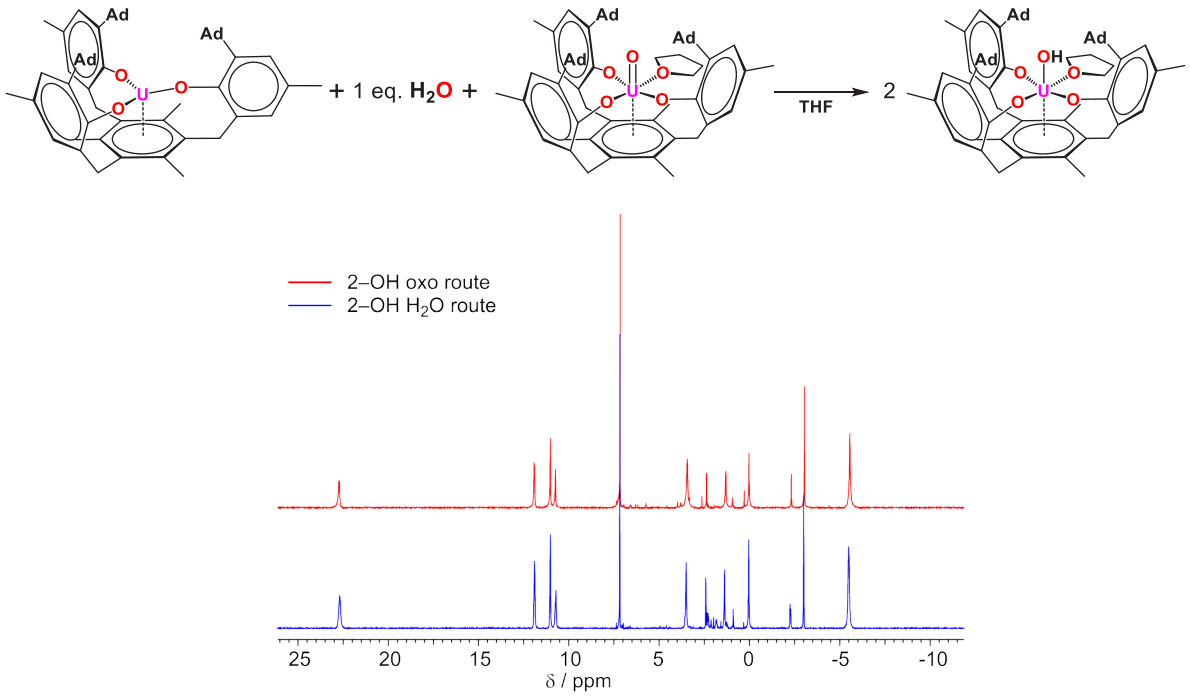

Fig. S4 | Upper panel: Reaction scheme depicting the role of the uranium oxo complex [((^{Ad,Me}(ArO$_3$)mes)U=O(THF)] during the synthesis of **2–OH** from **1** and H_2O, as predicted by the mechanism. Lower panel: ^{1}H NMR spectra confirming the formation of *two* eq. of [((^{Ad,Me}(ArO$_3$)mes)U(OH)(THF)] (**2-OH**), from the reaction of *one* eq. of [((^{AdMe}(ArO$_3$)mes)U] with *one* eq. of [((^{Ad,Me}(ArO$_3$)mes)U=O(THF)] and *one* eq. of H_2O.

Vis-NIR Spectroscopy

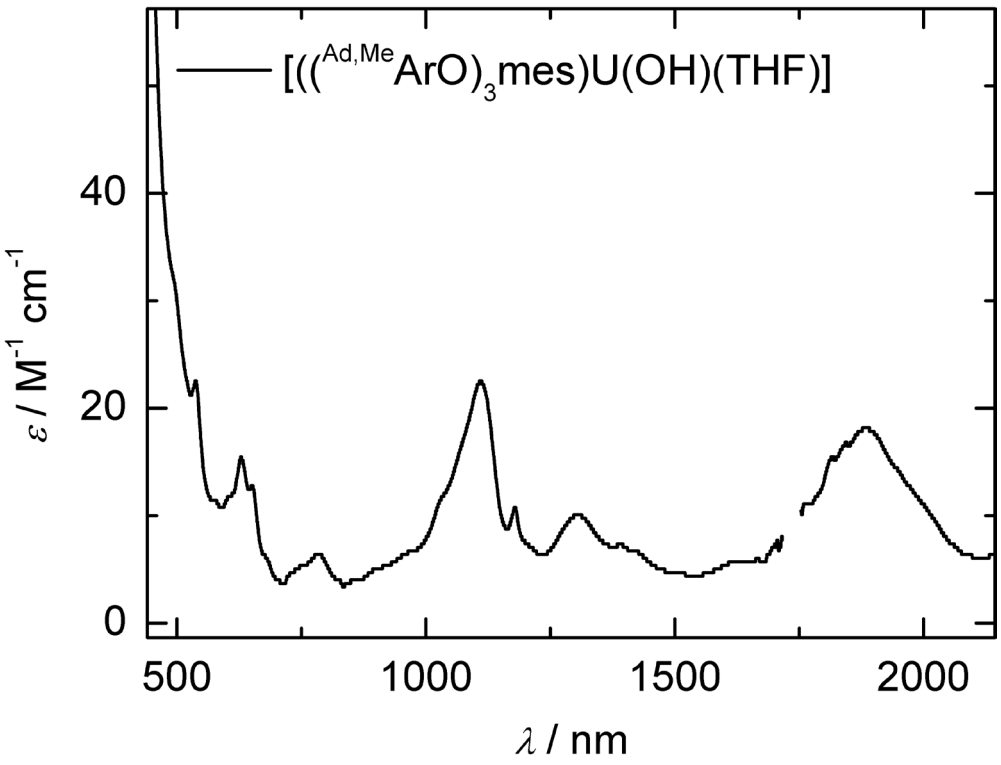

Fig. S5 | Vis-NIR spectrum of [[(^{Ad,Me}ArO)$_3$mes)U(OH)(THF)] **2–OH**, 3 mM in THF.

Table S 1 | Absorption band / extinction coefficient pairs for the electronic absorption spectrum of **2–OH** in THF.

λ /nm	537	629	651	784	1110	1179	1305	1887
ε / l mol^{-1} cm^{-1}	23	15	13	6	23	11	10	18

EPR Spectroscopy

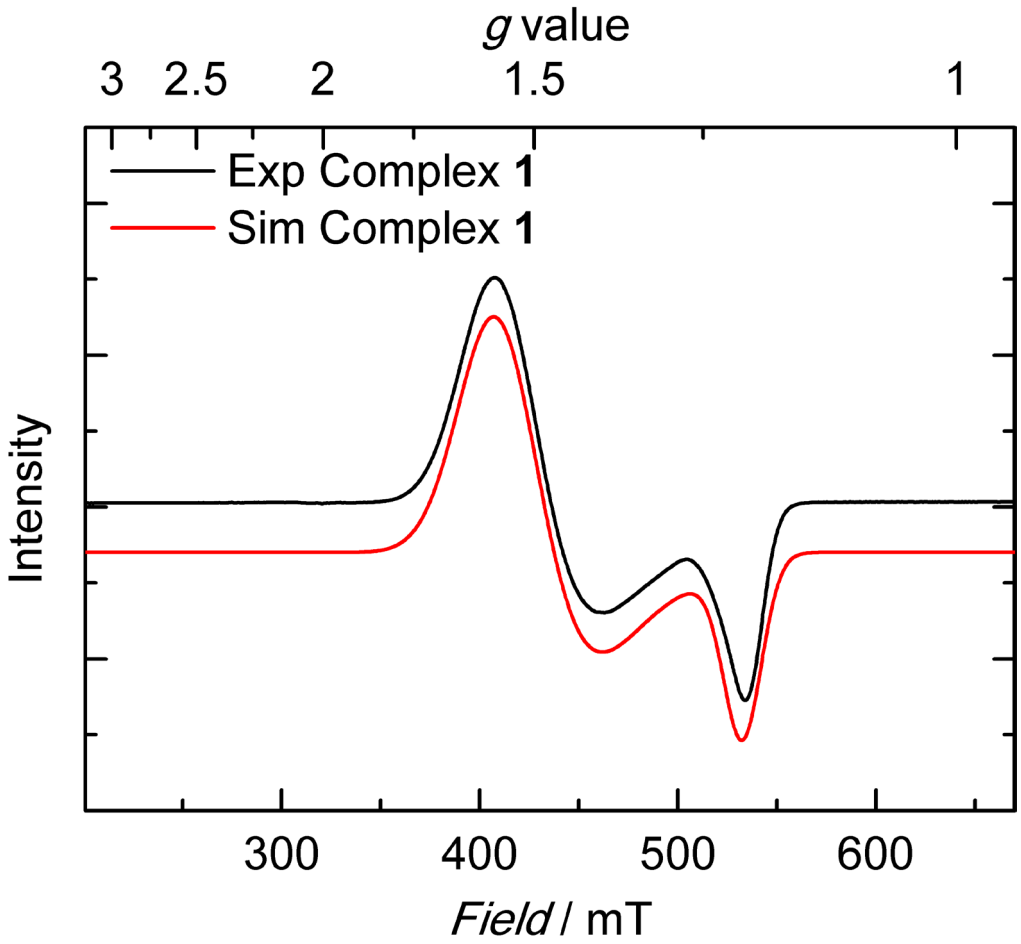

Fig. S6 | X Band EPR spectrum of the U(III) precursor **1**, recorded at 7.5 K in 10 mM in toluene (ν = 8.953288 GHz, P = 0.1 mW, modulation = 1.0 mT). The spectrum was simulated with g values of g_1 = 1.56, g_2 = 1.48, g_3 =1.20, and line widths of W_1 = 21.4, W_2 = 27.8 and W_3 = 11.1.

SQUID Magnetometry

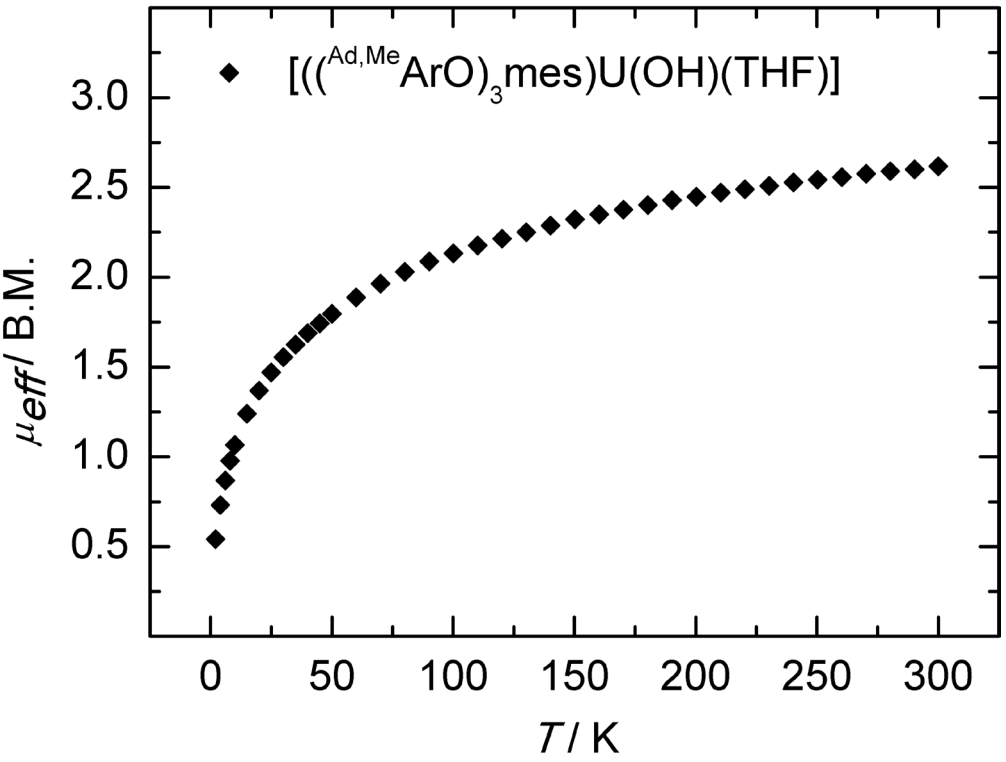

Fig. S7 | Temperature dependent SQUID measurement (1 T, 2 – 300 K) of a powdered sample of **2–OH** (17.0 mg).

Gas Chromatography

For the quantification of the H_2 content in the electrolysis cell head space, a calibration curve was prepared from multiple measurements with precisely adjusted H_2 concentrations in N_2. The obtained calibration curve is shown in Fig. S8. The faradaic efficiency of the electrocatalytic cycle was studied by gas chromatography coupled electrolysis experiments, where the passed charge was compared to the amount of H_2 detected in GC-TCD experiments. The electrolysis cell was a standard Schlenk tube, sealed with a rubber septum, through which all electrodes were passed into the sample solution. After the electrolysis, 100 µL of the headspace were injected into the gas chromatograph with a gas tight Hamilton syringe. Although great effort was made to seal the electrolysis cell, a H_2 leakage of 25% in 20 minutes was found in time dependent GC-TCD experiments, resulting in an observed faradaic yield way below 100%. In order to correct for the leakage, the same cell was equipped with a Pt working electrode to electrolyze an aqueous solution of 1.2 M NaOH for comparison. The electrolysis potential was adjusted such, that the constant electrolysis current was identical to the electrolysis current of the electrocatalytic H_2O reduction utilizing catalyst **1**. Indeed, identical H_2 content was found after identical electrolysis time (75 min) for the electrocatalytic cycle with **1**, and the platinum catalyzed NaOH electrolysis; thus, strongly suggesting identical faradaic yields for both systems. Qualitative H_2 evolution in stoichiometric reactions of **1** with H_2O to form **2–OH** was also confirmed by GC-TCD experiments. Therefore, the synthesis was conducted in a closed reaction vessel, which was sealed with a septum to take a sample of the headspace.

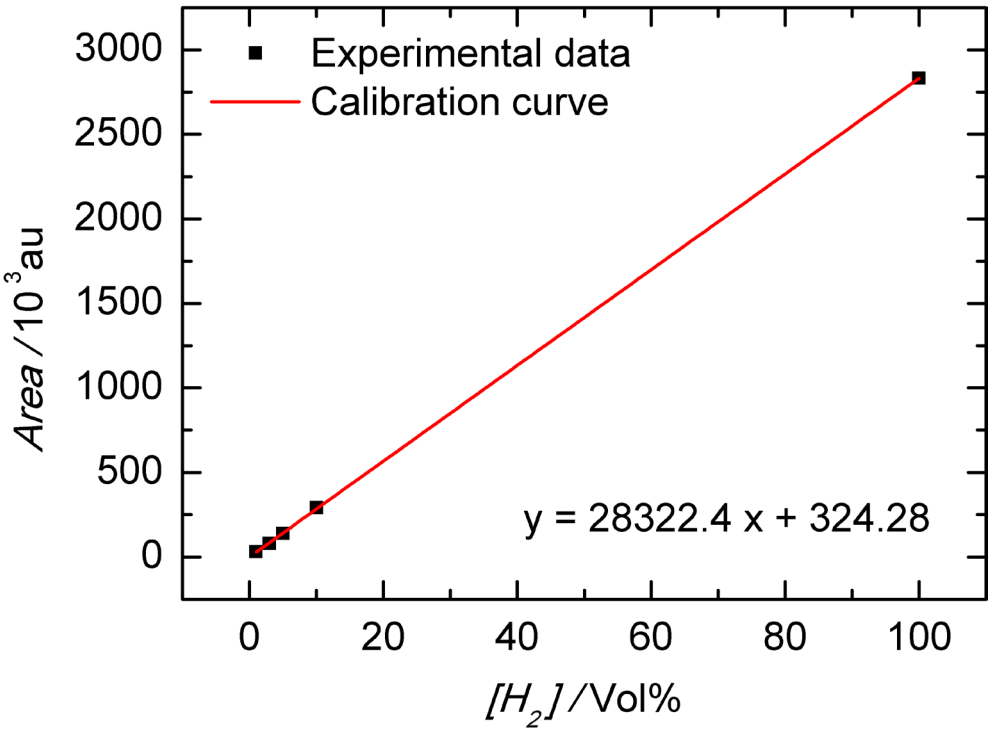

Fig. S8 | Calibration curve for quantitative H_2 determination, obtained from measurements of precisely prepared mixtures of H_2 and N_2, in gas collecting tubes, yielding H_2 volumetric concentrations of 1, 3, 5 ,10, and 100 % H_2 in N_2.

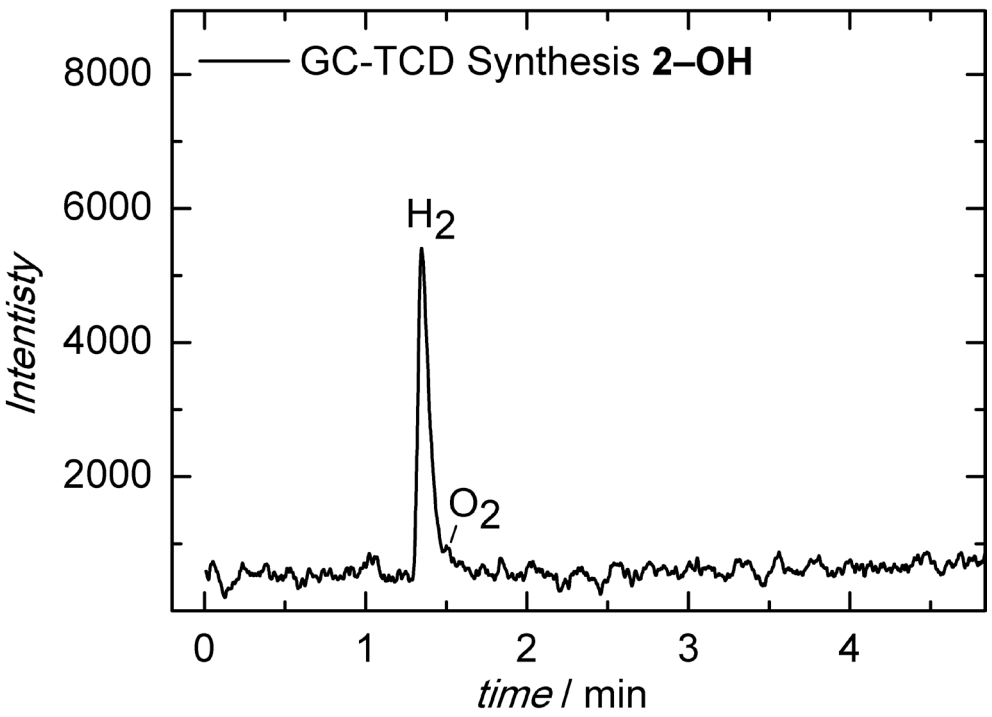

Fig. S9 | GC headspace analysis of the stoichiometric synthesis of **2–OH** from **1** with *one* eq. of H_2O in a sealed reaction vessel revealed the formation of H_2.

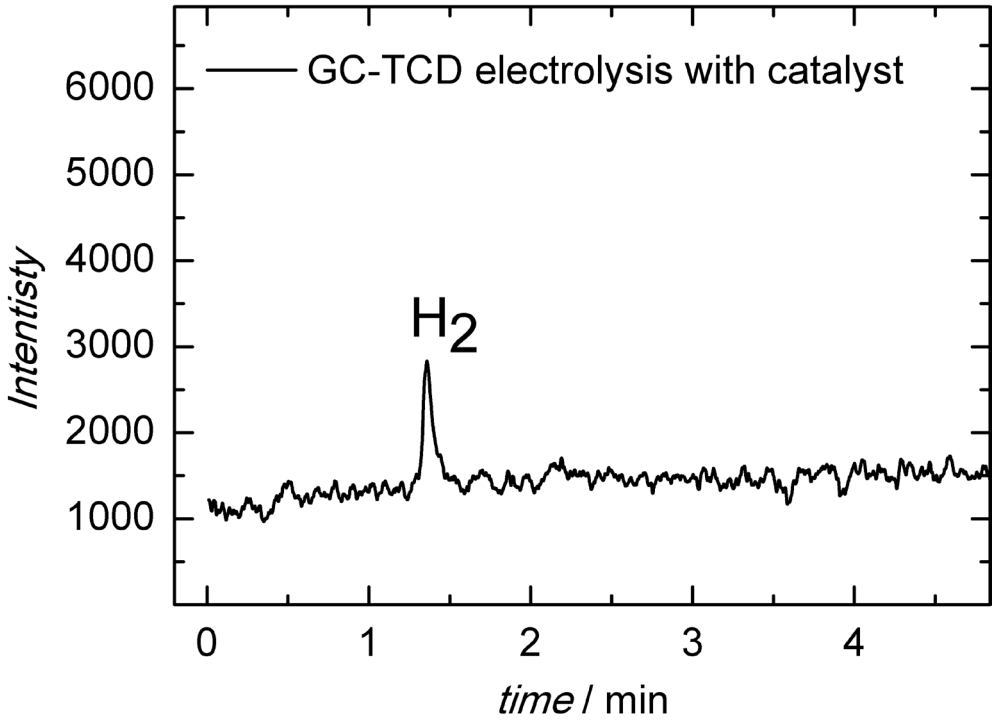

Fig. S10 | GC headspace analysis of electrocatalytic H_2O reduction in a sealed electrolysis cell including 5 mg of **1**, H_2O (0.22M in THF) and 5 mL THF.

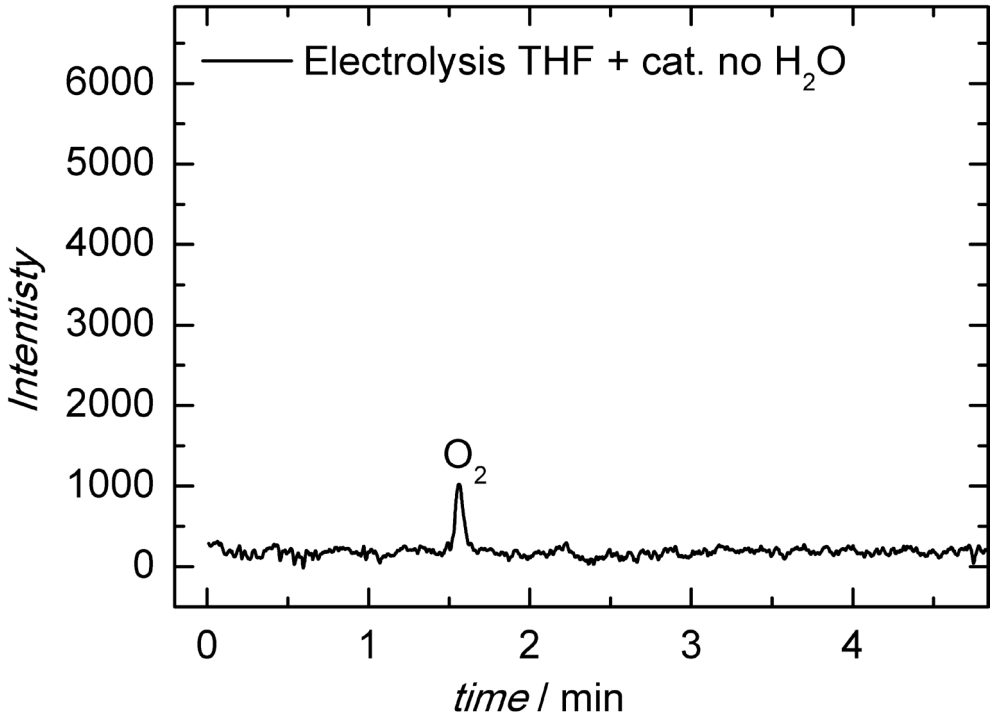

Fig. S11 | GC head space analysis of an electrolysis experiment with strict exclusion of H_2O in a sealed electrolysis cell including 5 mg of **1**, and 5 mL THF. The analysis proves that no H_2 is formed in the absence of the substrate H_2O by our catalyst.

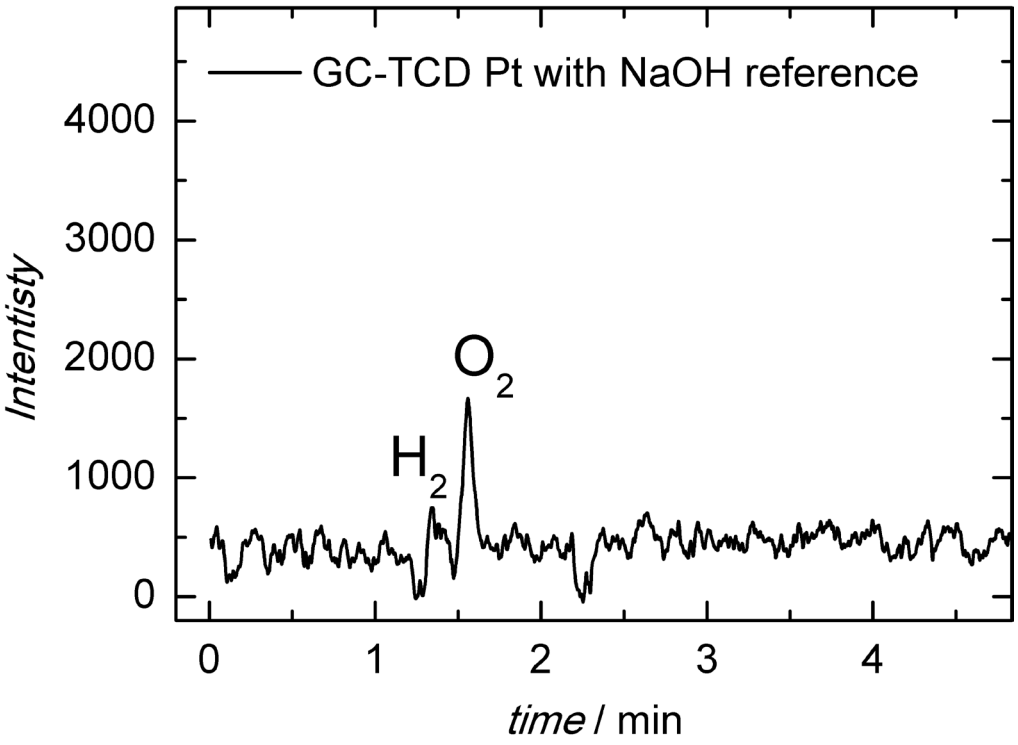

Fig. S12 | Reference electrolysis of NaOH (1.2 M in H_2O) with a Pt electrode under aerobic conditions to dertermine the H_2 gas leakage of the sealed cell. The hight of the oxygen peak is increased, since the electrolysis setup was assembled under air and then sealed for the electrolysis.

Electrochemical Studies

Amperometry

Amperometric experiments for bulk electrolyses were performed with a rotating disk glassy carbon working electrode (diameter 3 mm, stir rate 300 rad/s), a platinum rod counter electrode and a Ag wire reference electrode under inert gas conditions in a N_2 equipped glovebox, unless noted otherwise. The applied potential was –3.25 V *vs*. Fc^+/Fc, which was controlled by the addition of purified Fc to the sample solution and monitored by cyclic voltammetry. Electrolysis experiments for GC analysis were conducted in a standard Schlenk tube sealed with a rubber septum, through which all electrodes were passed into the sample solution. The electrolysis solution was then stirred with a glass stir bar (stir rate 300 rpm). The reference electrolysis of a 1.2 M NaOH solution was conducted in a Schlenk tube with a Pt disk working electrode (diameter 5 mm), a Pt rod counter electrode, and a Ag wire reference electrode and a glass stir bar. The potential is reported against the Ag^+/Ag couple, since ferrocene is not soluble in H_2O.

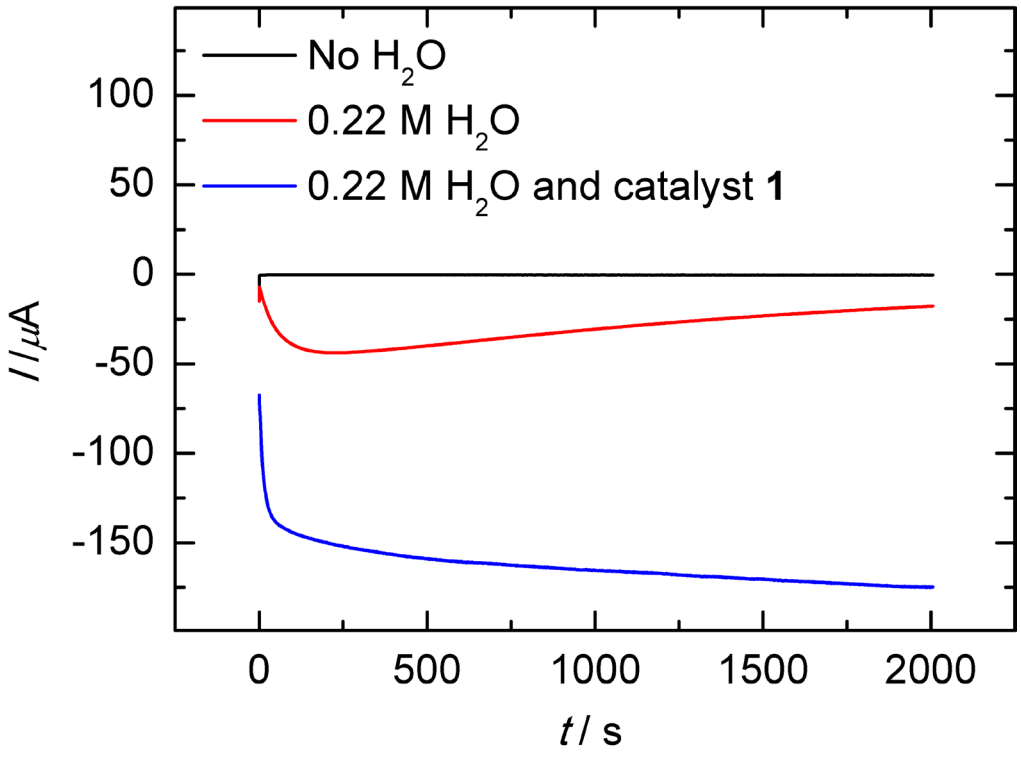

Fig. S13 | Chrono amperometry experiments with a rotating disk glassy carbon working electrode in THF with $TBAPF_6$, 0.1 M.

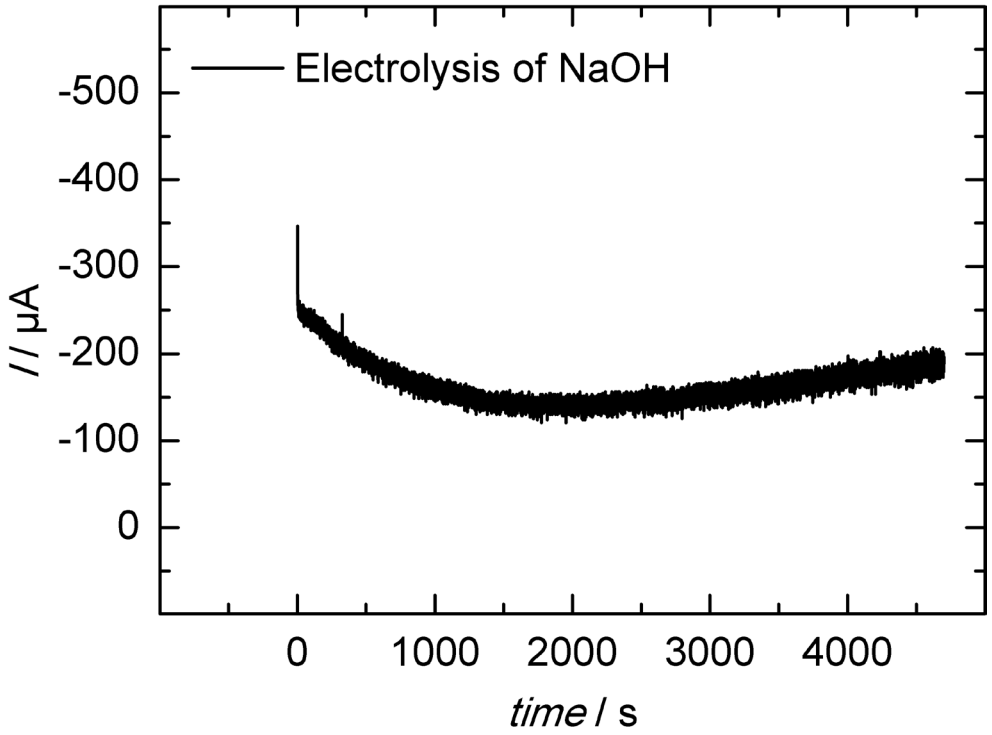

Fig. S14 | Chronoamperogram of NaOH electrolysis (1.2 M in H_2O), obtained at an electrolysis potential of –1.60 V vs Ag^+/Ag with a Pt disk electrode (diameter 5mm), a Pt rod counter electrode, and a Ag wire reference electrode.

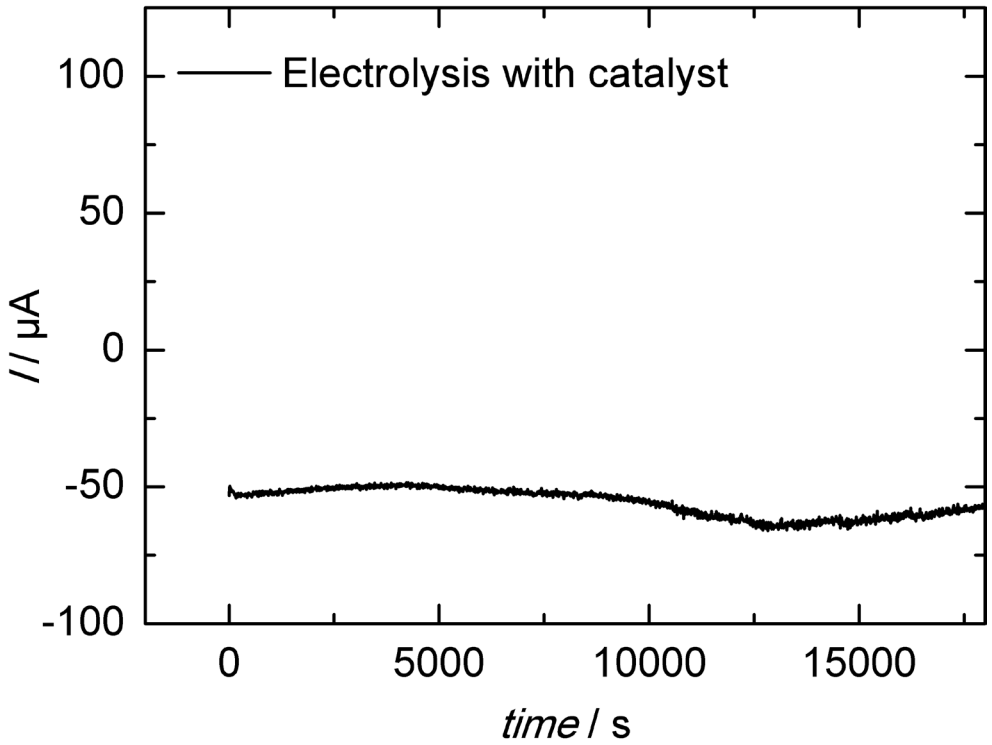

Fig. S15 | Chronoamperogram of H_2O electrolysis (0.22 M in THF) catalyzed by **1** at an electrolysis potential of –3.25 V *vs.* Fc^+/Fc with a glassy carbon disk working electrode (3 mm), a Pt rod counter electrode and a Ag wire reference electrode in THF with 0.1 M $TBAPF_6$.

Electrochemical Impedance Spectroscopy

The experimental data for the catalyzed H_2O reduction were fitted with a Randles equivalent circuit between 880.429 Hz and 0.122888 Hz, yielding a cell resistance R_s = 2.564 kΩ, a faradaic resistance R_{ct} = 3.704 kΩ, and a double layer capacity C_{dl} = 6.422 x 10^{-7} F. The experimental data for un-catalyzed H_2O electrolysis were fitted with two Randles equivalent circuits in series between 880.429 Hz and 0.0262447 Hz, yielding a cell resistances R_s = 3.203 kΩ, faradaic resistances R_{ct1} = 122.6 kΩ, R_{ct2} = 1.232 MΩ, as well as double layer capacities C_{dl1} = 2.446 x 10^{-6} F and C_{dl2} = 4.772 x 10^{-6} F.

Squarewave Voltammetry

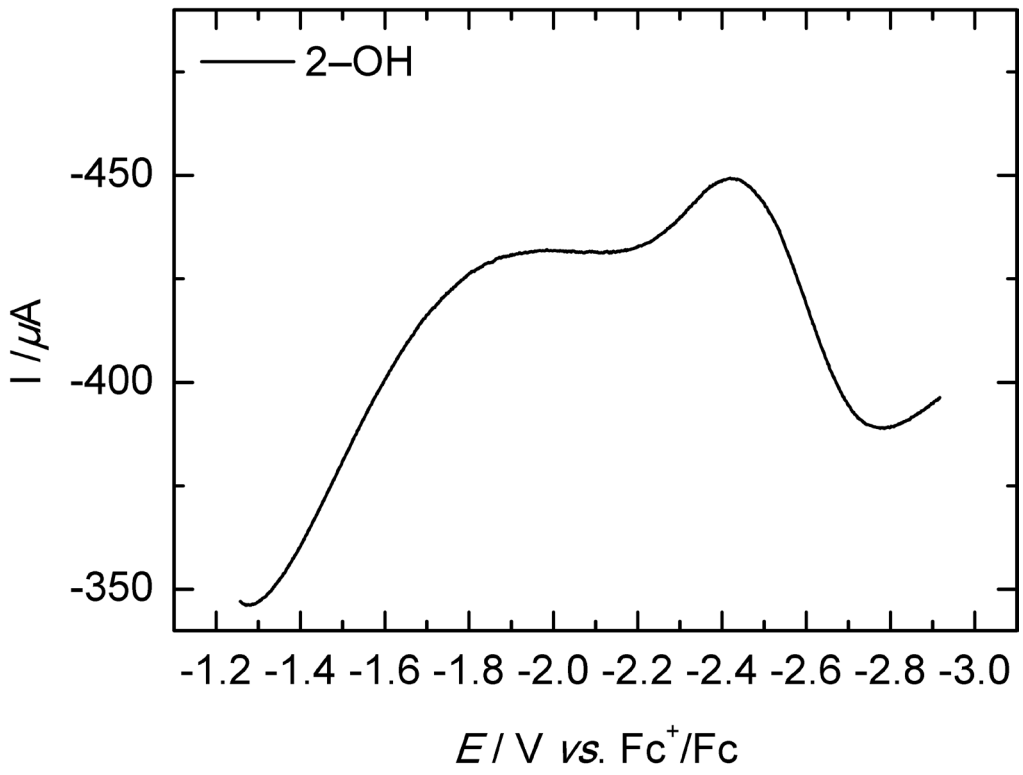

Fig. S16 | Square wave voltammogram of **2–OH** in THF with 0.1 M $TBAPF_6$. Two independent reduction events, centered around –1.9 V and –2.5 V are resolved.

Open Circuit Potential Measurement

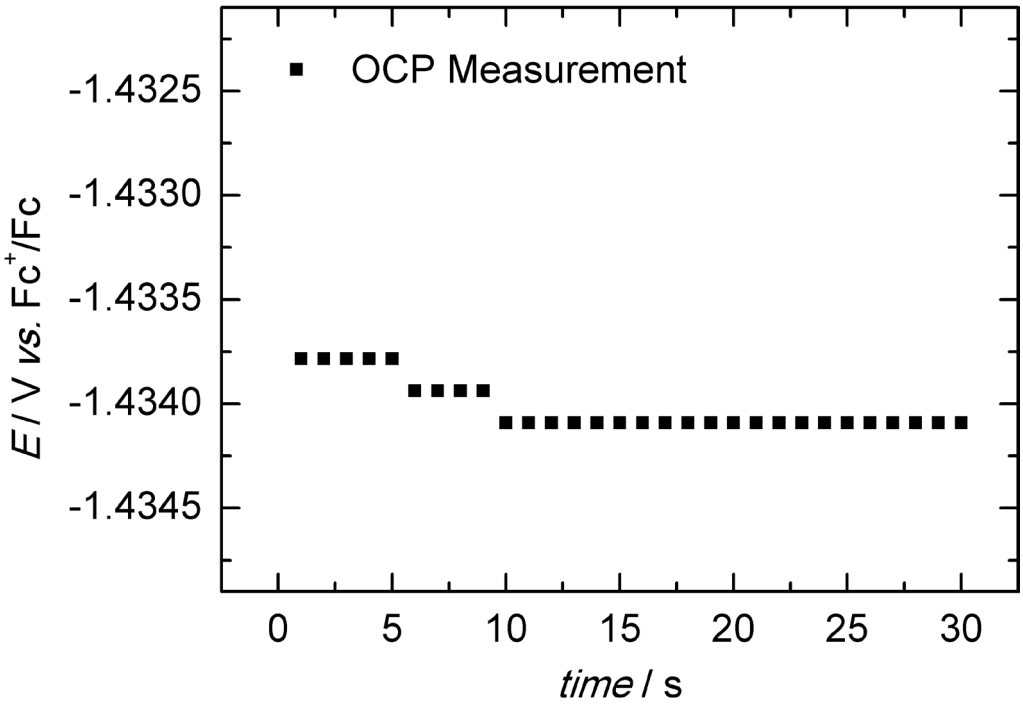

Fig. S17 | OCP Measurement for the determination of the thermodynamic potential for H_2 formation, as introduced by Bullock *et al.* [2], measured with a platinized Pt electrode, a Pt counter electrode, and a Ag wire pseudo reference electrode in a solution of 0.22 M H_2O in THF with 0.1 M $TBAPF_6$ measured under 1 atm. of H_2.

Cyclic Voltammetry

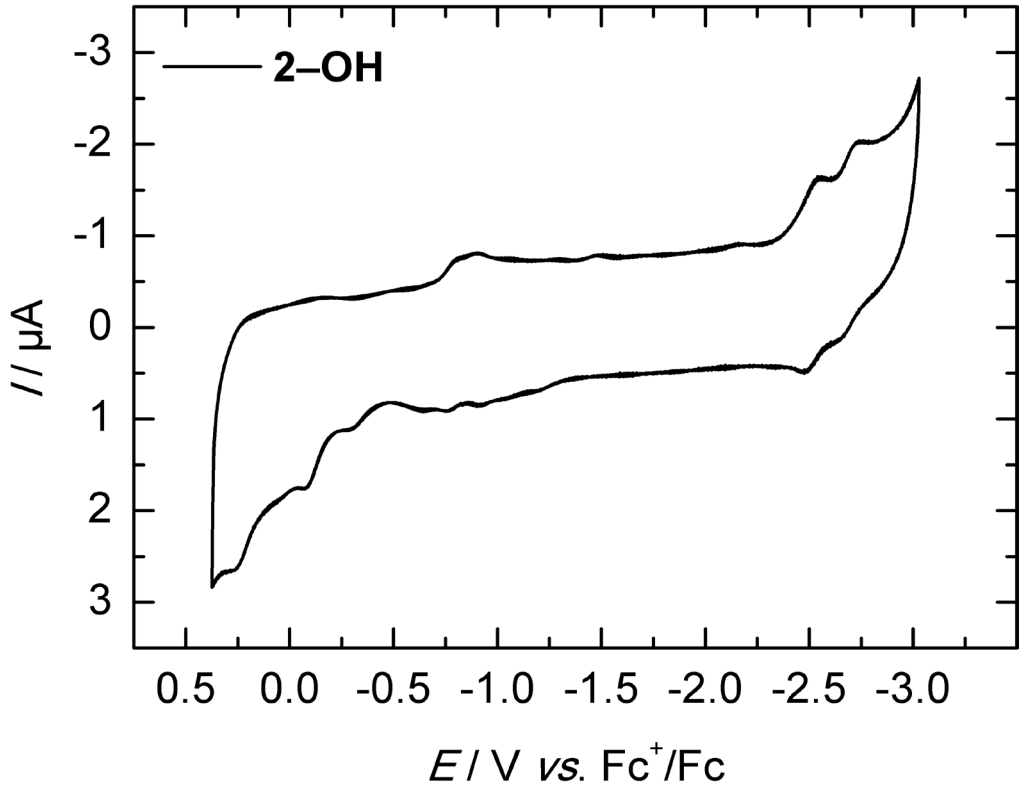

Fig. S18 | Cyclic voltammogram of **2–OH** in THF with 0.1 M $TBAPF_6$.

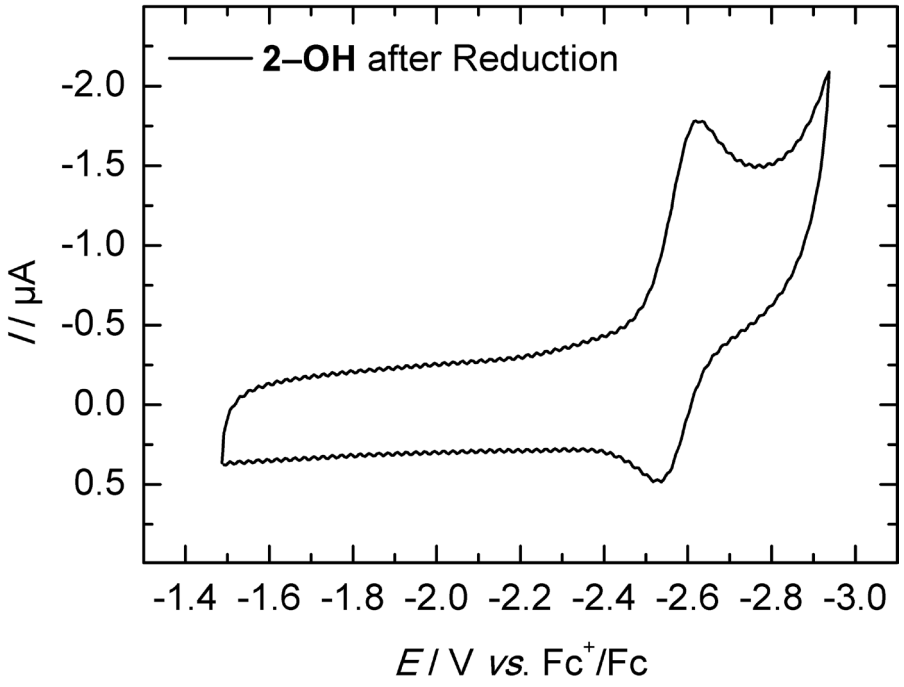

Fig. S19 | Cyclic voltammogram of the U(III)/U(II) redox couple of electrochemically generated **1** from an initially pure sample of **2–OH** (electrolysis at –2.2 V *vs*. Fc^+/Fc) in THF with 0.1 M $TBAPF_6$.

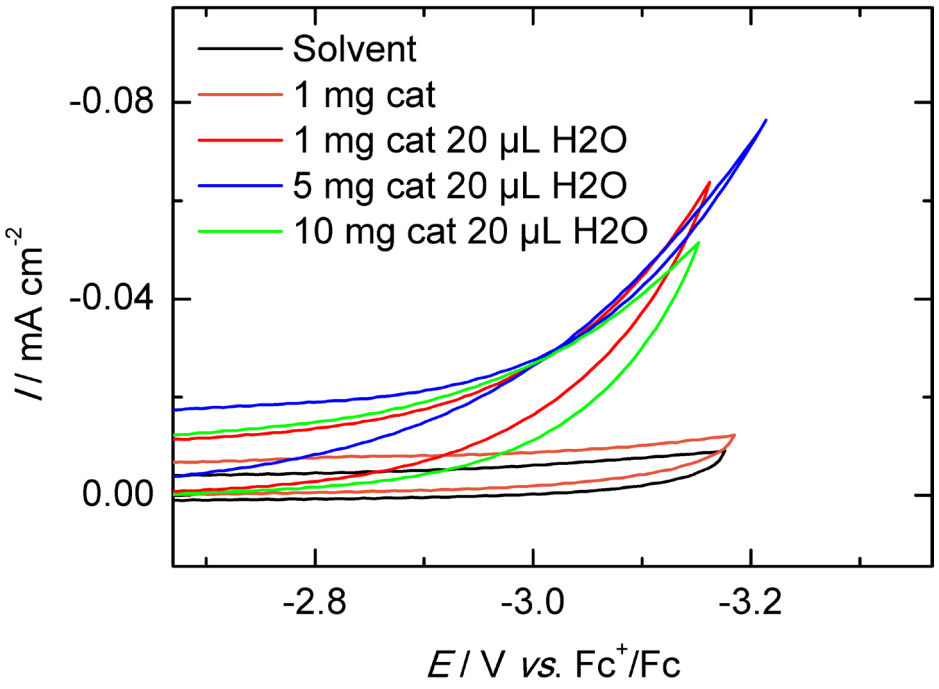

Fig. S20 | Cyclic voltammograms of electrocatalytic H_2O reduction with increasing concentrations of the catalyst, recorded with a glassy carbon working electrode in THF with 0.1 M $TBAPF_6$. The overlay shows neither a decrease of the onset potential, nor an increased catalytic current for higher catalyst concentrations.

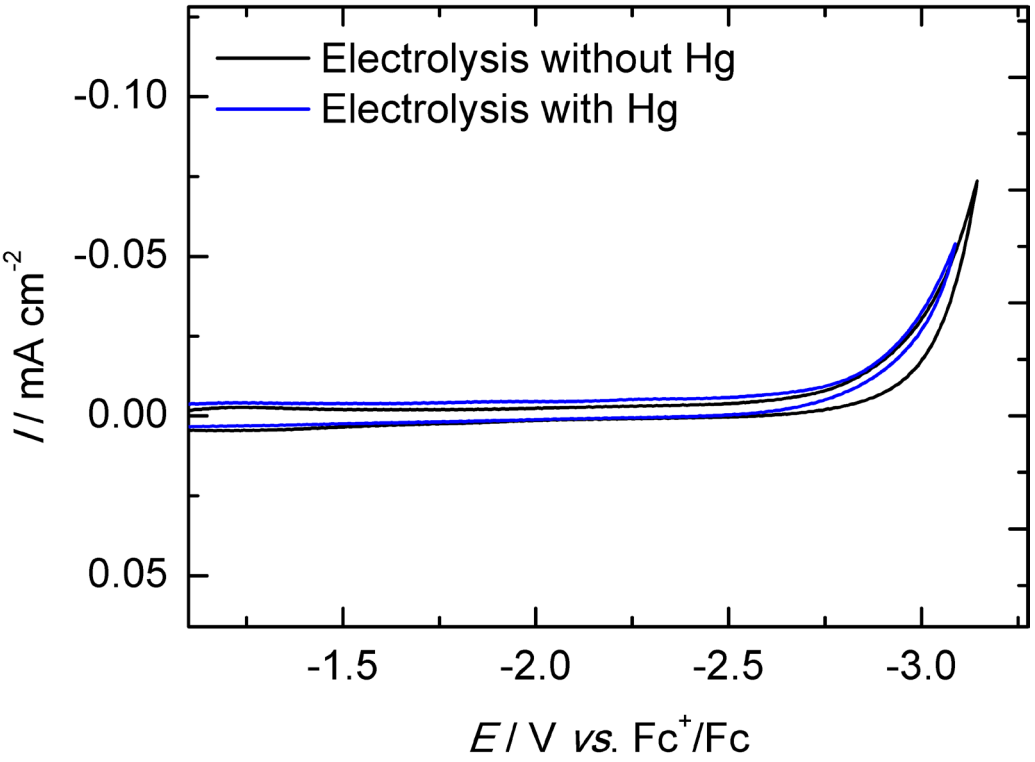

Fig. S21 | CV analysis of electrocatalytic H_2O reduction (0.22 M in THF) with 5 mg of catalyst **1** in 5 mL THF with 0.1 M $TBAPF_6$, with (blue trace) and without (black trace) the addition of an excess of Hg. The analysis shows that the addition of Hg did neither influence the onset potential or the catalytic current response for H_2O reduction with catalyst **1**, hinting that no catalytically active nanoparticles are present.

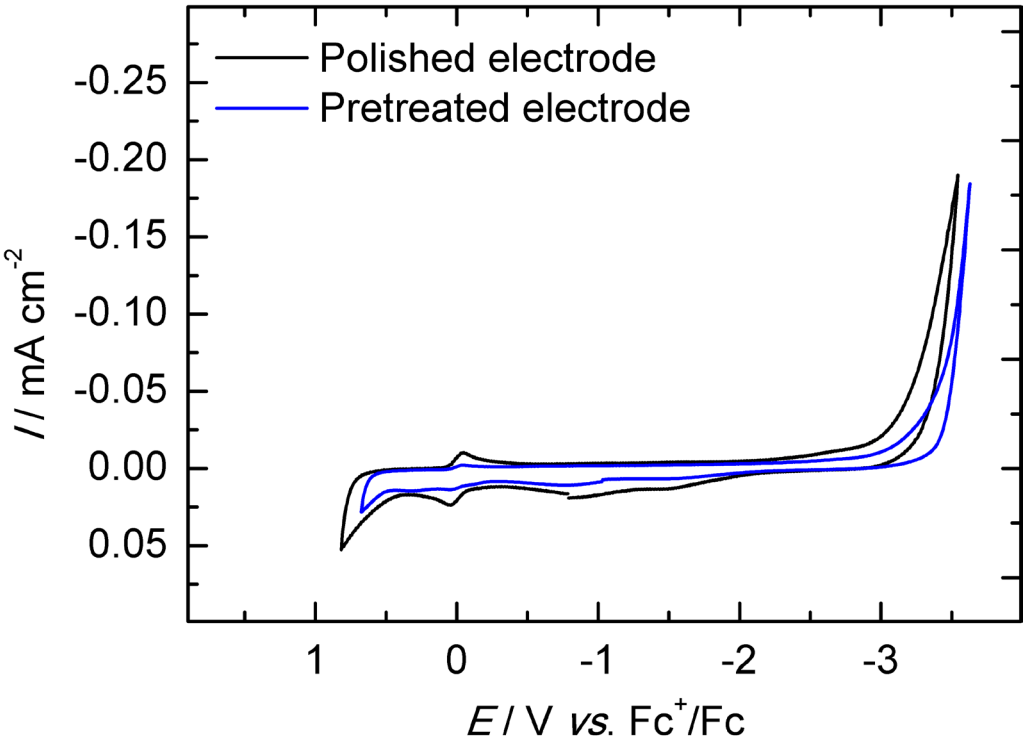

Fig. S22 | Cyclic voltammograms of a solution containing 0.22 M H_2O in THF with 0.1 M $TBAPF_6$, recorded with a freshly polished electrode (black trace) and an electrode that was pre-treated by multi-hour electrolysis in a solution containing catalyst **1** and, subsequently, carefully rinsed with THF prior to use. The overlay plot shows neither a decrease of the onset potential, nor an increased current for the pre-treated electrode. Hence, a catalytically active film is most likely not produced during the electrolysis with catalyst **1**.

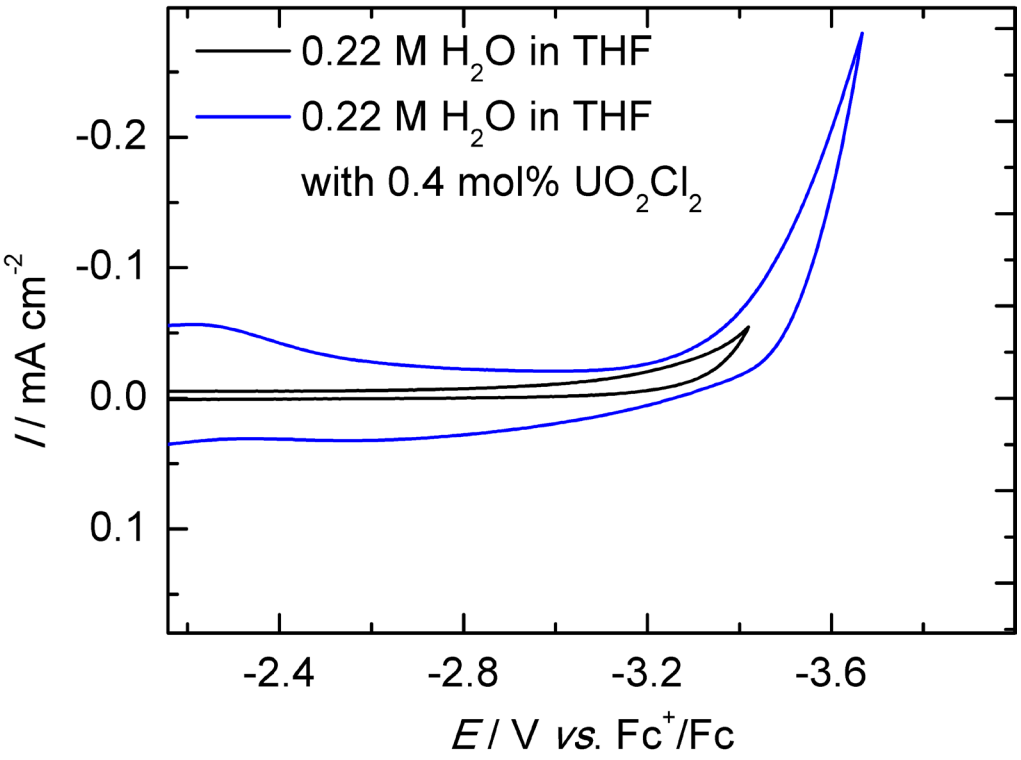

Fig. S23 | Cyclic Voltammograms of H_2O reduction (0.22 M in THF) in the presence (blue trace) and absence (black trace) of the uranly salt UO_2Cl_2 (0.4 mol % - the standard catalyst loading). No change of the onset potential or the catalytic current was observed in the presence of uranyl; hence, the catalytic activity observed for catalyst **1** is unlikely to originate from potential decomposition products, which are most typically uranyl salts.

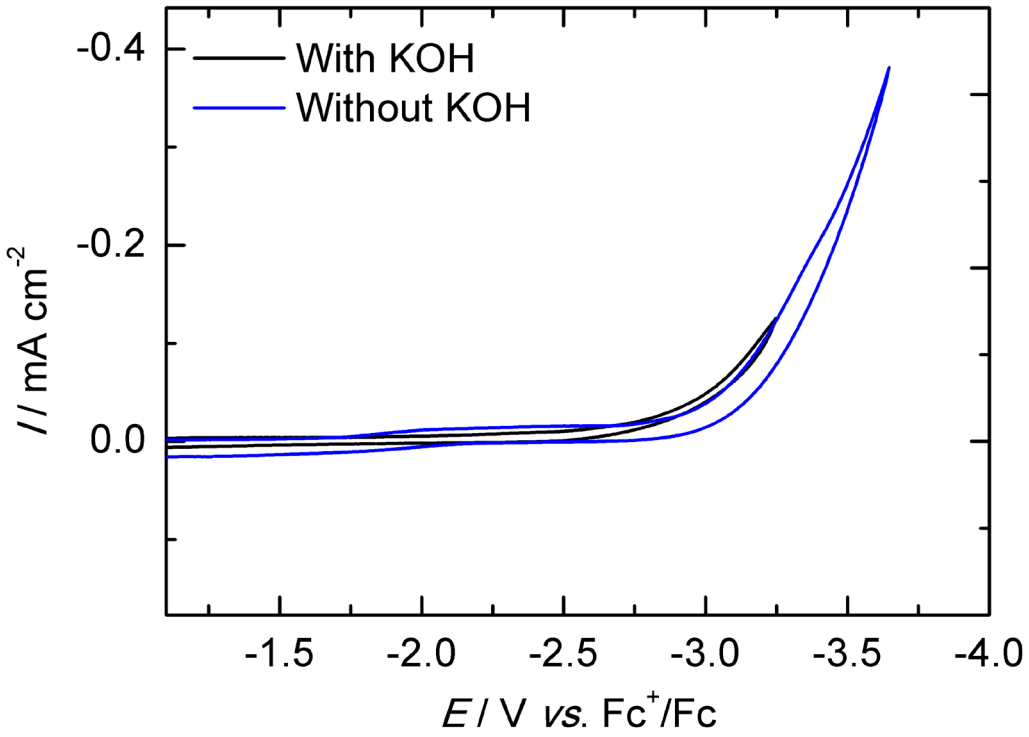

Fig. S24 | CV analysis of electrocatalytic H_2O reduction (0.22 M in THF) with 5 mg of catalyst **1** in 5 mL THF with 0.1 M $TBAPF_6$ with (black trace) and without (blue trace) the addition of an excess of solid KOH. The analysis clearly shows that the addition of KOH did neither influence the onset potential or the catalytic current response for H_2O reduction with catalyst **1**.

Direct Comparison of Catalyst 1 and the Mo-Based Catalyst $[(PY5Me_2)MoO](B(C_6H_3(CF_3)_2)_4)_2$

In order to provide further comparability to transition metal based catalysts, our catalyst was compared to the catalyst reported by J. Long & C. Chang *et al.* [3], which was tested under identical experimental conditions to our catalyst, with comparable results for the overpotential and the catalytic current response.

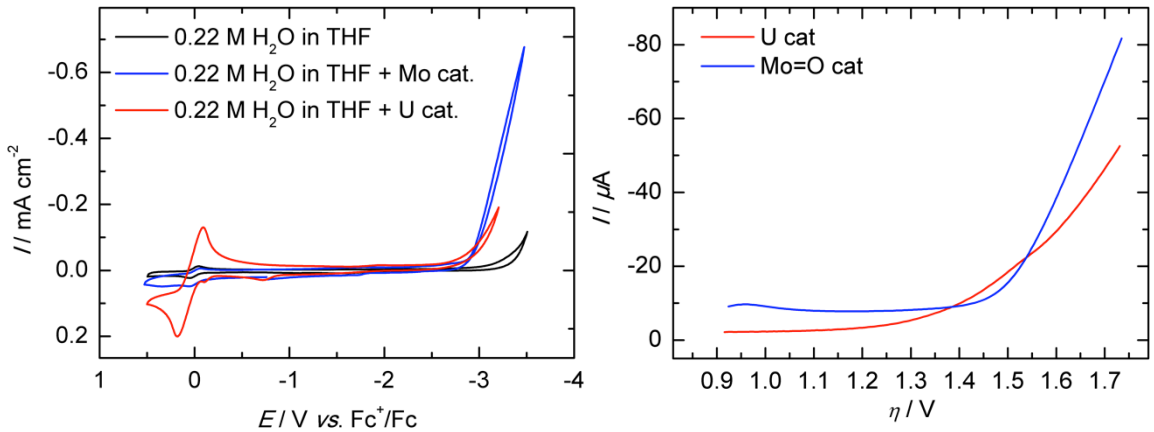

Fig. S25 | *Left*: Cyclic voltammograms showing H_2O (0.22 M in THF) reduction without a catalyst (black trace), with the Mo=O catalyst, $[(PY5Me_2)MoO]^{2+}$ ($7 \cdot 10^{-4}$ M) reported by J. Long & C. Chang (Mo cat, blue trace), and with the U catalyst **1** ($9 \cdot 10^{-4}$M) (U cat, red trace), recorded with a glassy carbon working electrode in THF with 0.1 M $TBAPF_6$. *Right*: I *vs.* η plots for $[(PY5Me_2)MoO]^{2+}$ (blue trace) and the U catalyst **1** (red trace).

Foot-of-the-wave Analysis

A foot-of-the-wave analysis was performed for our catalyst **1**, as reported by Savéant *et al.* [4] and Dempsey *et al.* [5], yielding a TOF of 10^6 h^{-1} (at η = 1.3 V) for our experimental conditions.

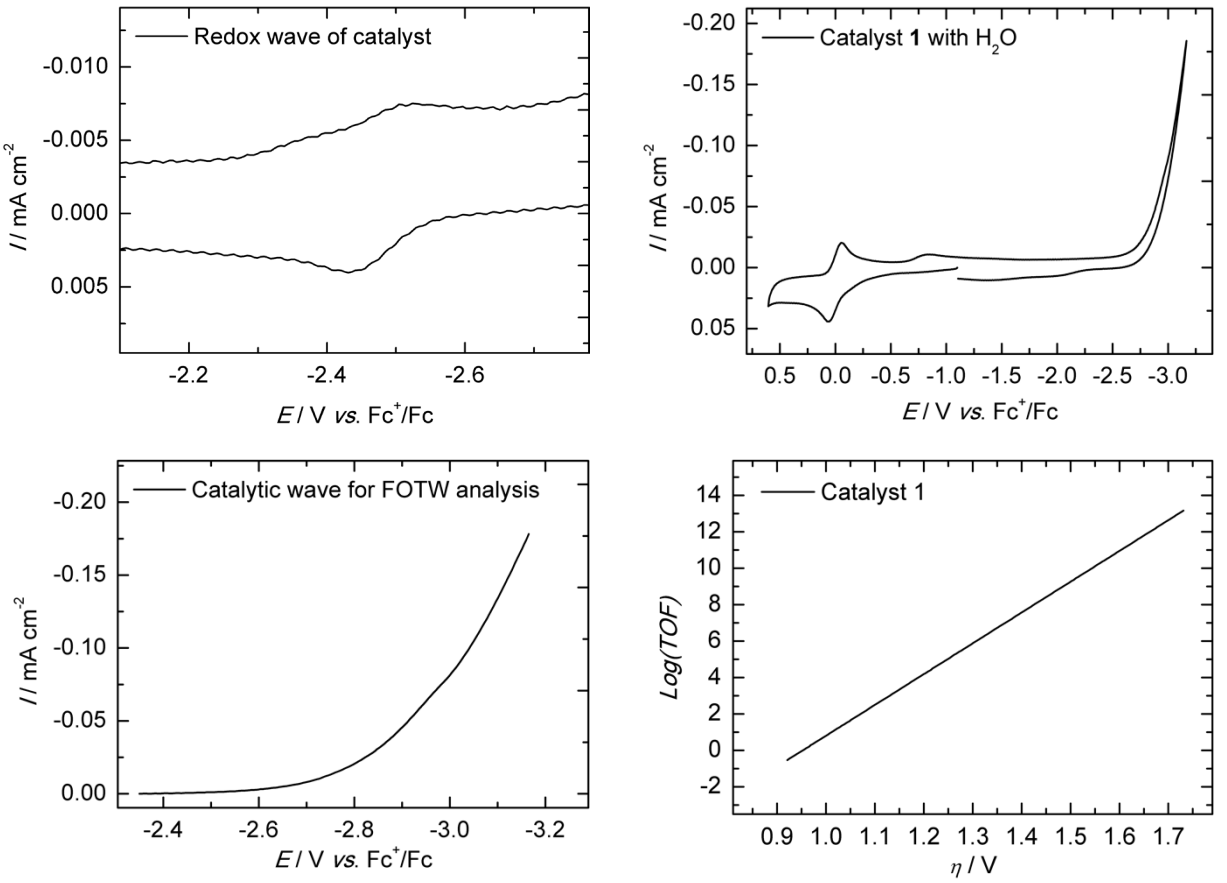

$$\frac{i}{i_p^0} = \frac{2.24\sqrt{\frac{RT}{F\nu}2k}}{1+\exp\left[\frac{F}{RT}\left(E-E_{pQ}^0\right)\right]}$$

$$k = \frac{m^2 \cdot \nu \cdot F}{RT + 10.0352}$$

with:
I = catalytic current
I_p^0 = peak current of catalyst
$E^0_{P/Q}$ = halfwave potential of catalyst wave
ν = scanrate
m = slope of FOTW analysis graph

Fig. S26 | *Top, left*: Redox wave of catalyst **1**, recorded from 1 mg catalyst in 5 mL THF with 0.1 M $TBAPF_6$, yielding E^0_{PQ} and I^0_p. *Top right*: Catalytic H_2O (0.22 M) reduction with 1 mg catalyst in 5 mL THF with 0.1 M $TBAPF_6$, including a Fc^+/Fc wave set to 0 V for referencing. *Middle left*: Referenced catalytic wave for foot-of-the-wave analysis. *Middle right*: Log(TOF) *vs.* η plot for catalyst **1**. *Lower panels*: equations used for the foot-of-the-wave-analysis.

X-Ray Crystal Structure Determination

CCDC-1413741 (for **2–OH** from THF/*n*-pentane), CCDC-1401838 (for **2–OH** from THF), and CCDC-1437872 (for [((^{Ad,tBu}ArO)$_3$tacn)U(OH)] · 2Et$_2$O) contain the supplementary crystallographic data for this paper. This data can be obtained free of charge *via*

http://www.ccdc.cam.ac.uk/products/csd/request/ (or from Cambridge Crystallographic Data Centre, 12 Union Road, Cambridge, CB2 1EZ, UK (fax: ++44-1223-336-033; e-mail: deposit@ccdc.cam.ac.uk).

Table S2 | Crystallographic data, data collection and refinement details of **2–OH** from THF/*n*-pentane and **2-OH** from THF.

	2–OH from THF/*n*-pentane	**2–OH** from THF	$[U(OH)((^{Ad}ArO)_3tacn)] \cdot 2Et_2O$
Empirical formula	$C_{79}H_{108}O_8U$	$C_{80.69}H_{111.38}O_{8.42}U$	$C_{77}H_{117}N_3O_6U$
Mol. weight	1423.68	1454.14	1418.76
Crystal shape, color	plate, yellow	plate, yellow	plate, colorless
Crystal size [mm]	0.24×0.08×0.06	0.15×0.14×0.03	0.17×0.11×0.05
Temperature [K]	100(2)	100(2)	100(2)
Crystal system	Monoclinic	Monoclinic	Monoclinic
Space group	*C*2/*c*	*C*2/*c*	$P2_1/c$
a [Å]	41.806(5)	30.480(4)	10.937(2)
b [Å]	15.940(2)	15.941(2)	30.067(6)
c [Å]	24.293(3)	27.850(3)	22.150(4)
α [°]	90	90	90
+β [°]	124.082(2)	97.786(2)	94.76(3)
γ [°]	90	90	90
V [Å^3]	13408(3)	13407(3)	7259(3)
Z	8	8	4
ρ [g cm^{-3}] (calc.)	1.411	1.441	1.298
μ [mm^{-1}]	2.478	2.481	2.288
F (000)	5904	6039	2960
T_{min}; T_{max}	0.635 0.746	0.646 0.746	0.322 0.894
2*Θ* interval [°]	3.0 ≤ 2*Θ* ≤ 57.5	2.6 ≤ 2*Θ* ≤ 55.9	6.0 ≤ 2*Θ* ≤ 51.4
Coll. refl.	102606	106770	95932
Indep. refl.; R_{int}	17424; 0.0571	16057; 0.0701	13759; 0.1944
Obs. refl. $F_0 \geq 4\sigma(F)$	13973	11953	8553
No. ref. param.	937	1165	877
wR_2 (all data)	0.0746	0.1002	0.2189
R_1 ($F_0 \geq 4\sigma(F)$)	0.0301	0.0386	0.0849
GooF on F^2	1.059	1.071	1.065
$\Delta\rho_{max/min}$	1.078; –0.793	1.353; –0.991	2.684; –2.977

Table S3 | Selected bond distances [Å] and angles [°] for **2–OH** from THF/*n*-pentane with e.s.d.'s in parentheses.

Bond distances			
U1—O1	2.191 (2)	C1—C2	1.406 (4)
U1—O2	2.205 (2)	C1—C6	1.415 (4)
U1—O3	2.167 (2)	C1—C10	1.514 (4)
U1—O4	2.616 (2)	C2—C3	1.409 (4)
U1—O5	2.106 (2)	C2—C7	1.512 (4)
U1—C1	3.009 (3)	C3—C4	1.412 (4)
U1—C2	3.014 (3)	C3—C28	1.512 (4)
U1—C3	3.066 (3)	C4—C5	1.399 (4)
U1—C5	3.026 (3)	C4—C8	1.513 (4)
U1—C6	2.994 (3)	C5—C6	1.410 (4)
O1—C12	1.360 (3)	C5—C46	1.518 (4)
O2—C30	1.349 (3)	C6—C9	1.510 (4)
O3—C48	1.351 (3)		
O4—C64	1.442 (4)		
O4—C67	1.453 (4)		
O5—H5	1.05		
Bond angles			
O1—U1—O2	106.15 (7)	C2—U1—C3	26.78 (8)
O1—U1—O3	153.49 (7)	C2—U1—C5	55.78 (8)
O1—U1—O4	79.36 (7)	C2—U1—C6	48.01 (8)
O1—U1—C1	63.63 (7)	C3—U1—C5	47.08 (8)
O1—U1—C2	77.45 (7)	C6—U1—C3	55.20 (8)
O1—U1—C3	104.24 (7)	C6—U1—C5	27.09 (7)
O1—U1—C5	105.31 (7)	C12—O1—U1	155.5 (2)
O1—U1—C6	78.23 (7)	C30—O2—U1	160.3 (2)
O2—U1—O4	169.90 (7)	C48—O3—U1	161.6 (2)
O2—U1—C1	98.16 (8)	C64—O4—U1	125.9 (2)
O2—U1—C2	71.74 (8)	C64—O4—C67	105.4 (2)
O2—U1—C3	63.97 (7)	C67—O4—U1	118.8 (2)
O2—U1—C5	108.84 (8)	U1—O5—H5	139.0
O2—U1—C6	117.67 (7)	C2—C1—U1	76.7 (2)
O3—U1—O2	100.31 (7)	C2—C1—C6	120.1 (3)
O3—U1—O4	74.72 (7)	C2—C1—C10	119.5 (3)
O3—U1—C1	109.7 (2)	C6—C1—U1	75.8 (2)
O3—U1—C2	111.42 (7)	C6—C1—C10	120.3 (3)
O3—U1—C3	85.88(8)	C10—C1—U1	121.6 (2)
O3—U1—C5	63.68 (7)	C1—C2—U1	76.3 (2)
O3—U1—C6	88.28 (7)	C1—C2—C3	119.4 (3)
O4—U1—C1	91.87 (7)	C1—C2—C7	119.8 (3)
O4—U1—C2	118.11 (7)	C3—C2—U1	78.7 (2)
O4—U1—C3	123.53 (7)	C3—C2—C7	120.7 (3)
O4—U1—C5	77.15 (7)	C7—C2—U1	118.5 (2)
		C2—C3—U1	74.6 (2)

O4—U1—C6	71.42 (7)	C2—C3—C4	120.1 (3)
O5—U1—O1	93.28 (7)	C2—C3—C28	122.2 (3)
O5—U1—O2	91.25 (8)	C4—C3—U1	81.2 (2)
O5—U1—O3	87.59 (7)	C4—C3—C28	117.6 (3)
O5—U1—O4	79.87 (2)	C28—C3—U1	117.8 (3)
O5—U1—C1	156.67 (8)	C3—C4—C5	119.9 (3)
O5—U1—C2	157.03 (8)	C8—C4—C3	120.1 (3)
O5—U1—C3	152.65 (8)	C8—C4—C5	119.9 (3)
O5—U1—C5	146.97 (8)	C4—C5—U1	82.9 (2)
O5—U1—C6	151.06 (8)	C4—C5—C46	120.5 (3)
C1—U1—C2	27.01 (8)	C6—C5—U1	75.2 (2)
C1—U1—C3	47.16 (8)	C6—C5—C4	119.4 (3)
C1—U1—C5	47.82 (8)	C6—C5—C46	120.0 (3)
C1—U1—C6	27.26 (8)	C46—C5—U1	112.6 (2)
		C1—C6—U1	77.0 (2)
		C1—C6—C9	120.3 (3)
		C5—C6—U1	77.7 (2)
		C5—C6—C1	120.0 (3)
		C5—C6—C9	119.4 (3)
		C9—C6—U1	121.7 (2)

Table S4 | Selected bond distances [Å] and angles [°] for **2–OH** from THF with e.s.d.'s in parentheses.

Bond distances			
U1—O1	2.180 (3)	C1—C2	1.3900
U1—O2	2.211 (3)	C1—C6	1.3900
U1—O3	2.181 (3)	C1—C10	1.527 (15)
U1—O4	2.592 (3)	C2—C3	1.3900
U1—O5	2.110 (3)	C2—C7	1.547 (12)
U1—C1	2.903 (10)	C3—C4	1.3900
U1—C2	2.920 (8)	C3—C28	1.515 (12)
U1—C3	3.006 (8)	C4—C5	1.3900
U1—C5	3.057 (17)	C4—C8	1.314 (18)
U1—C6	2.973 (16)	C5—C6	1.3900
O1—C12	1.352 (5)	C5—C46	1.46 (2)
O2—C30	1.411 (7)	C6—C9	1.538 (18)
O3—C48	1.353 (5)		
O4—C64	1.456 (5)		
O4—C67	1.463 (5)		
O5—H5	0.8400		
Bond angles			
O1—U1—O2	101.32 (13)	C2—U1—C3	27.08 (7)
O1—U1—O3	154.37 (11)	C2—U1—C5	55.37 (18)

O1—U1—O4	76.42 (10)
O1—U1—C1	65.45 (19)
O1—U1—C2	74.65 (18)
O1—U1—C3	101.27 (19)
O1—U1—C5	110.7 (2)
O1—U1—C6	84.6 (3)
O2—U1—O4	173.78 (10)
O2—U1—C1	98.8 (2)
O2—U1—C2	71.34 (19)
O2—U1—C3	60.47 (16)
O2—U1—C5	103.8 (2)
O2—U1—C6	115.4 (2)
O3—U1—O2	104.31 (12)
O3—U1—O4	78.13 (10)
O3—U1—C1	109.7 (2)
O3—U1—C2	113.35 (16)
O3—U1—C3	91.0 (2)
O3—U1—C5	62.5 (2)
O3—U1—C6	84.1 (2)
O4—U1—C1	85.57 (19)
O4—U1—C2	113.18 (18)
O4—U1—C3	125.51 (16)
O4—U1—C5	82.4 (2)
O4—U1—C6	70.3 (2)
O5—U1—O1	91.17 (11)
O5—U1—O2	91.73 (12)
O5—U1—O3	88.48 (11)
O5—U1—O4	82.56 (10)
O5—U1—C1	155.76 (18)
O5—U1—C2	154.76 (16)
O5—U1—C3	151.14 (16)
O5—U1—C5	149.5 (2)
O5—U1—C6	152.8 (2)
C1—U1—C2	27.62 (8)
C1—U1—C3	48.05 (11)
C1—U1—C5	47.6 (2)
C1—U1—C6	27.33 (12)
C2—U1—C6	48.22 (15)
C3—U1—C5	46.78 (17)
C6—U1—C3	55.41 (17)
C6—U1—C5	26.61 (14)
C12—O1—U1	162.8 (3)
C30—O2—U1	156.1 (4)
C48—O3—U1	161.2 (3)
C64—O4—U1	124.7 (3)
C64—O4—C67	108.2 (3)
C67—O4—U1	125.8 (2)
U1—O5—H5	109.5
C2—C1—U1	76.9 (4)
C2—C1—C6	120.0
C2—C1—C10	119.5 (9)
C6—C1—U1	79.1 (5)
C6—C1—C10	120.0 (9)
C10—C1—U1	121.8 (7)
C1—C2—U1	75.5 (4)
C1—C2—C3	120.0
C1—C2—C7	119.3 (8)
C3—C2—U1	79.9 (3)
C3—C2—C7	120.7 (8)
C7—C2—U1	114.2 (5)
C2—C3—U1	73.0 (3)
C2—C3—C4	120.0
C2—C3—C28	118.5 (9)
C4—C3—U1	79.5 (4)
C4—C3—C28	120.9 (9)
C28—C3—U1	126.1 (5)
C3—C4—C5	120.0
C8—C4—C3	102.1 (9)
C8—C4—C5	137.9 (9)
C4—C5—U1	77.5 (3)
C4—C5—C46	118.1 (13)
C6—C5—U1	73.3 (3)
C6—C5—C4	120.0
C6—C5—C46	121.9 (13)
C46—C5—U1	119.7 (13)
C1—C6—U1	73.5 (4)
C1—C6—C9	119.3 (9)
C5—C6—U1	80.1 (3)
C5—C6—C1	120.0
C5—C6—C9	120.7 (10)
C9—C6—U1	118.3 (11)

Table S5 | Selected bond distances [Å] and angles [°] for [U(OH)((^{Ad}ArO)$_3$tacn)] · 2Et$_2$O with e.s.d.'s in parentheses.

Bond distances			
U1—O1	2.187 (7)	N1—C1	1.502 (13)
U1—O2	2.178 (7)	N1—C6	1.499 (12)
U1—O3	2.185 (8)	N1 – C7	1.502 (15)
U1—O4	2.112 (7)	N2 – C2	1.500 (12)
U1—N1	2.722 (8)	N2 – C3	1.498 (14)
U1 – N2	2.731 (8)	N2 – C28	1.511 (12)
U1 – N3	2.716 (8)	N3 – C4	1.487 (13)
O1—C9	1.335 (12)	N3 – C5	1.465 (13)
O2—C30	1.341 (12)	N3 – C49	1.506 (12)
O3—C51	1.337 (12)		
O4—H4	0.8400		
Bond angles			
O1—U1—N1	69.4 (2)	C2—N2—U1	114.7 (6)
O1—U1—N2	132.4 (2)	C2—N2—C28	110.4 (8)
O1—U1—N3	84.6 (3)	C3—N2—U1	105.5 (5)
O2—U1—O1	119.3 (3)	C3—N2—C2	110.8 (8)
O2—U1—O3	117.5 (3)	C3—N2—C28	107.2 (8)
O2—U1—N1	84.4 (3)	C28—N2—U1	107.9 (5)
O2—U1—N2	68.6 (2)	C4—N3—U1	115.7 (6)
O2—U1—N3	131.8 (2)	C4—N3—C49	110.1 (9)
O3—U1—O1	120.7 (3)	C5—N3—U1	105.5 (6)
O3—U1—N1	132.4 (3)	C5—N3—C4	111.5 (8)
O3—U1—N2	83.8 (3)	C5—N3—C49	108.1 (8)
O3—U1—N3	70.2 (3)	C49—N3—U1	105.5 (6)
O4—U1—O1	83.3 (3)	C2—C1—N1	114.1 (9)
O4—U1—O2	85.2 (3)	C1—C2—N2	113.5 (8)
O4—U1—O3	85.5 (3)	N2—C3—C4	112.9 (9)
O4—U1—N1	140.8 (3)	N3—C4—C3	113.3 (8)
O4—U1—N2	142.6 (2)	N3—C5—C6	113.2 (8)
O4—U1—N3	141.9 (3)	N1—C6—C5	112.7 (8)
N1—U1—N2	64.7 (3)	C8—C7—N1	115.9 (9)
N3—U1—N1	64.5 (3)	C9—C8—C7	119.4 (9)
N3—U1—N2	65.0 (3)	C13—C8—C7	119.2 (9)
C9—O1—U1	151.5 (6)	C13—C8—C9	121.1 (10)
C30—O2—U1	153.4 (7)	O1—C9—C8	118.3 (9)
C51—O3—U1	151.4 (6)	O1—C9—C10	123.2 (9)
U1—O4—H4	109.5	C8—C9—C10	118.5 (10)
C1—N1—U1	105.2 (6)	C9—C10—C14	120.4 (10)
C1—N1—C7	106.8 (8)	C11—C10—C9	118.5 (10)
C6—N1—U1	114.7 (6)	C11—C10—C14	121.1 (10)
C6—N1—C1	111.1 (8)	C29—C28—N2	115.1 (9)
C6—N1—C7	111.9 (8)	O2—C30—C29	117.1 (10)
C7—N1—U1	106.6 (5)	O2—C30—C31	122.8 (10)
		C50—C49—N3	117.5 (9)

	O3—C51—C50 117.6 (9) O3—C51—C52 121.9 (9)

Graphical representations.

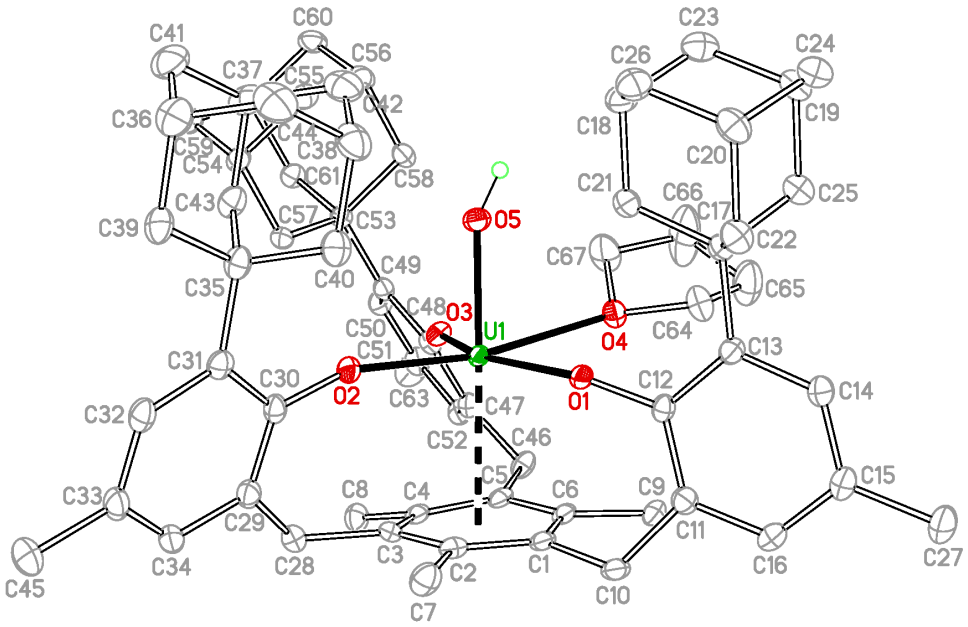

Fig. S27 | Molecular structure of **2–OH** from THF/*n*-pentane with the applied numbering scheme (50 % probability ellipsoids, minor fraction of the disorder, hydrogen atoms except for the hydroxo H and solvent molecules omitted for clarity).

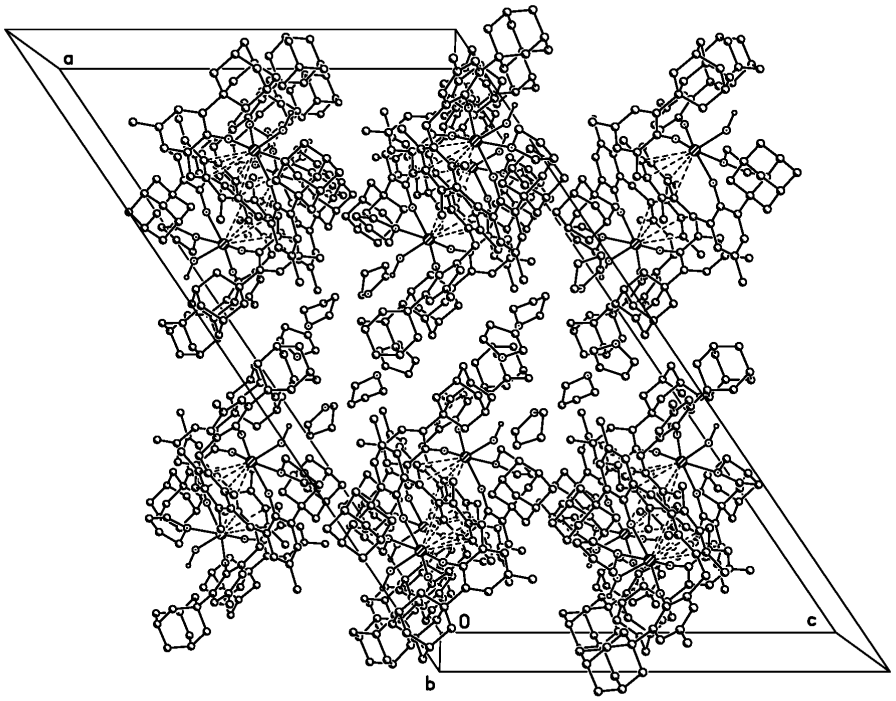

Fig. S28 | Crystal packing diagram for **2–OH** from THF/*n*-pentane (view along the crystallographic *b*-axis).

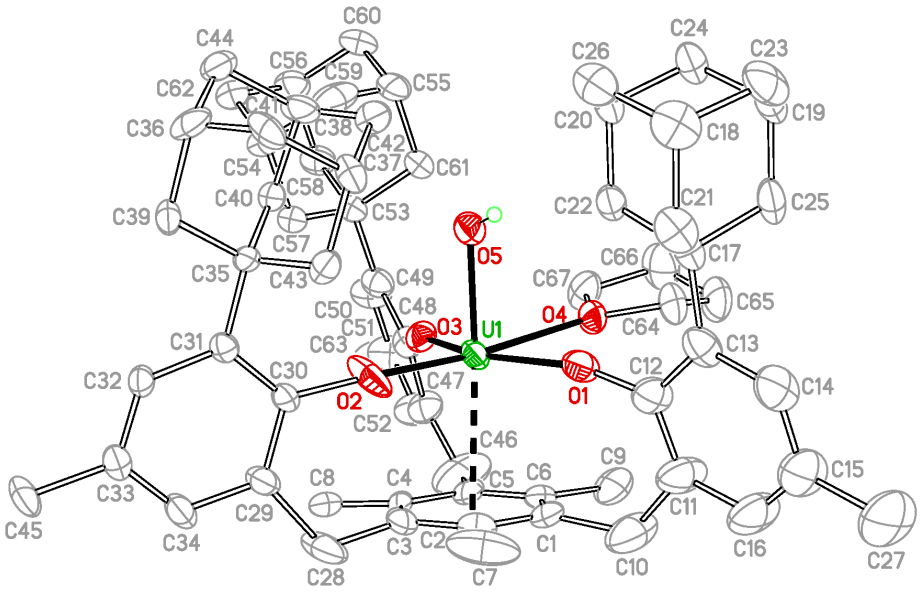

Fig. S29 | Molecular structure of **2–OH** from THF with the applied numbering scheme (50 % probability ellipsoids, minor fraction of the disorder, hydrogen atoms except for the hydroxo H and solvent molecules omitted for clarity).

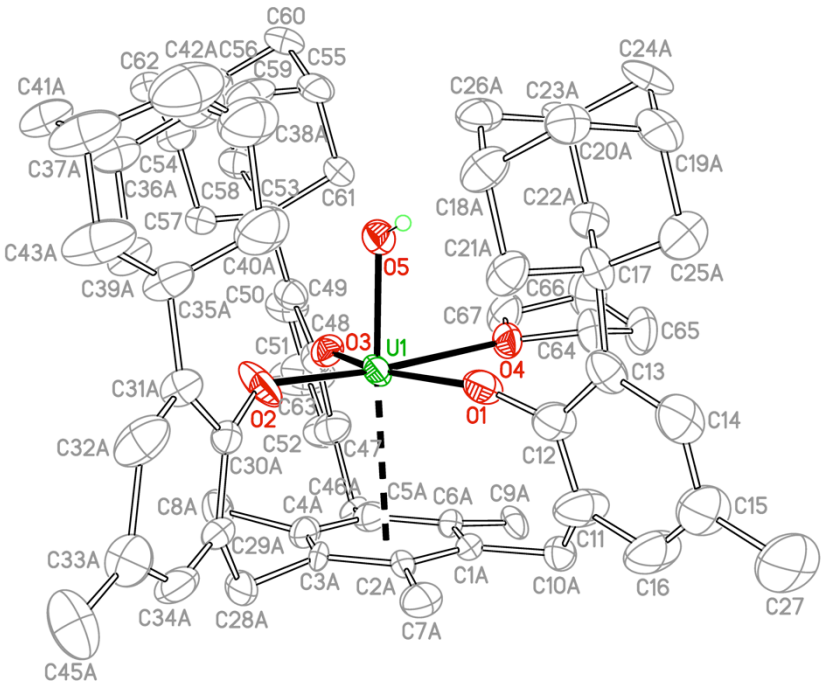

Fig. S30 | Molecular structure of **2–OH** from THF showing the alternative orientation of the ligand (minor fraction) with the applied numbering scheme (50 % probability ellipsoids, major fraction of the disorder, hydrogen atoms except for the hydroxo H and solvent molecules omitted for clarity).

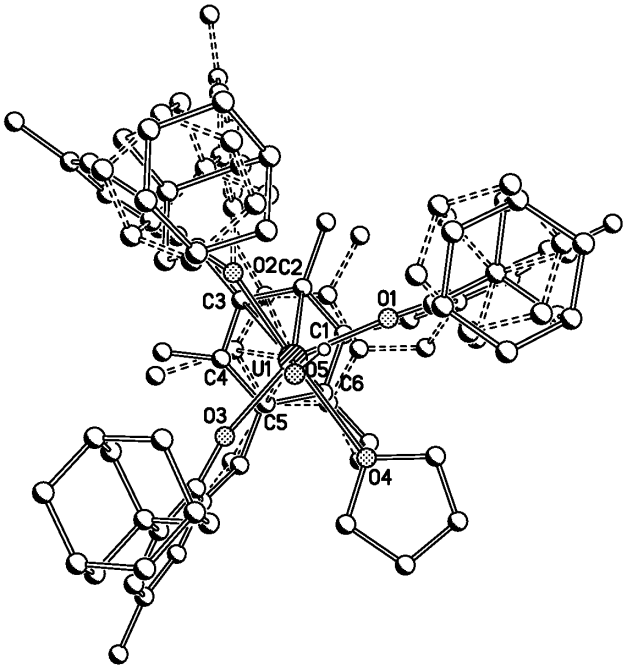

Fig. S31 | Top view of an overlay of the two alternative orientations of the molecular structure of **2–OH** from THF (the minor fraction is indicated by dashed bonds, hydrogen atoms except for the hydroxo H and solvent molecules omitted for clarity).

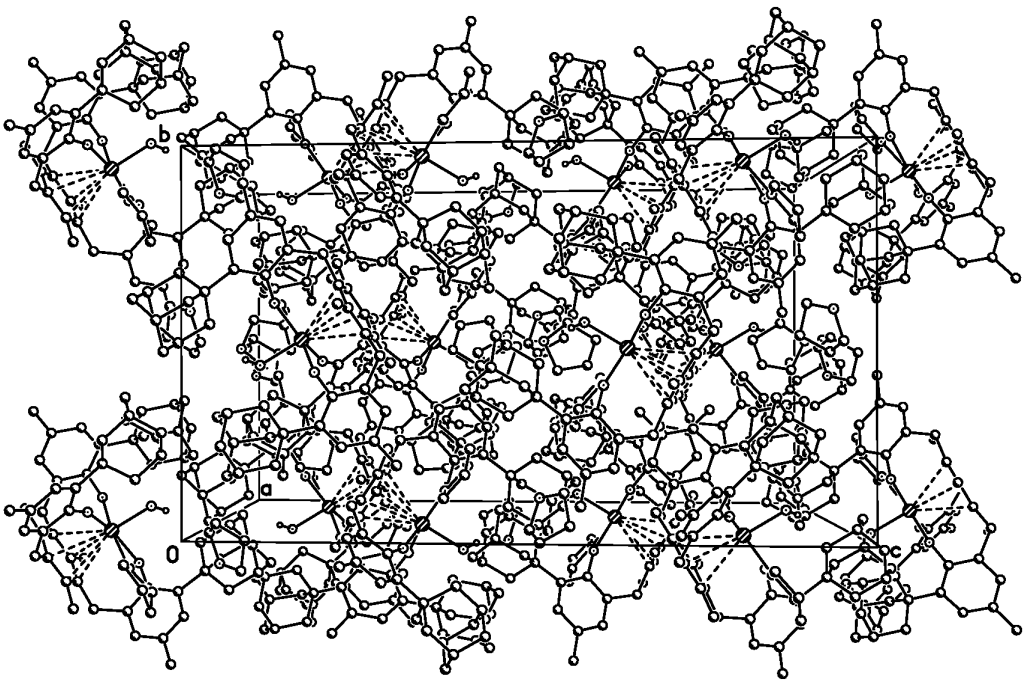

Fig. S32 | Crystal packing diagram for **2–OH** from THF (view along the crystallographic *a*-axis).

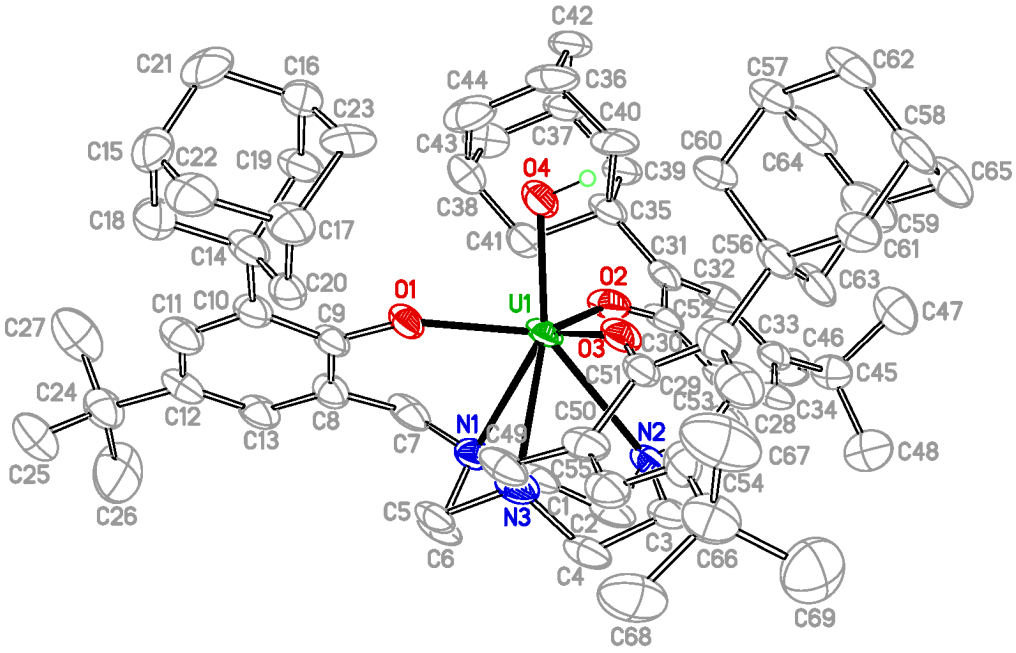

Fig. S33 | Molecular structure of [U(OH)((^{Ad}ArO)$_3$tacn)] with the applied numbering scheme (50 % probability ellipsoids, minor fraction of the disorder, hydrogen atoms except for the hydroxo H and solvent molecules omitted for clarity).

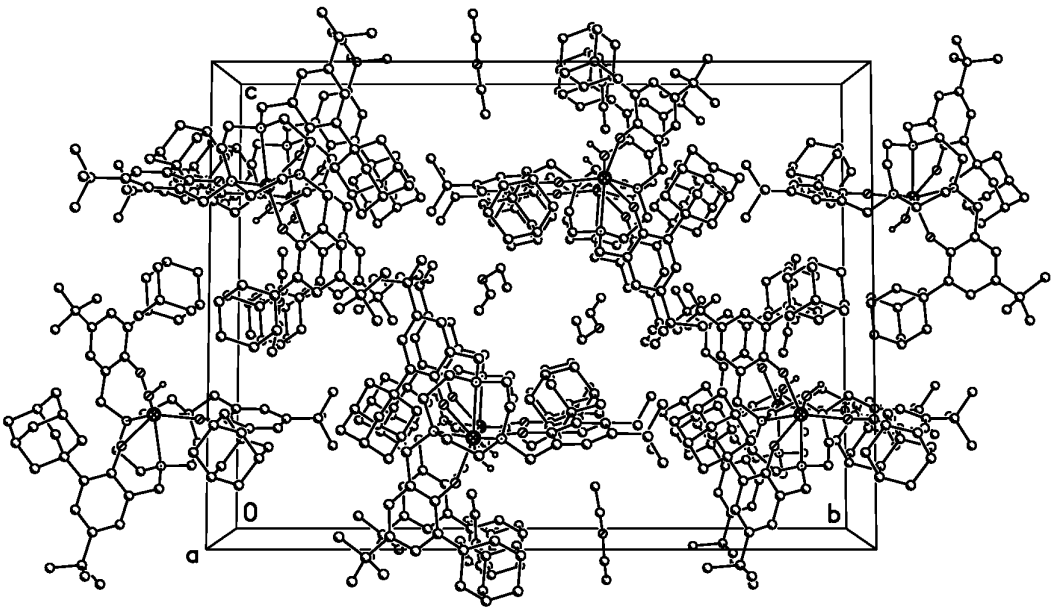

Fig. S34 | Crystal packing diagram for [U(OH)((^{Ad}ArO)$_3$tacn)] · 2Et$_2$O (view along the crystallographic *a*-axis).

References

1. Miller, A. C., Stewart, M., Brooks, K., Shi, L. & Page, N. Depleted uranium-catalyzed oxidative DNA damage: absence of significant alpha particle decay. *Journal of Inorganic Biochemistry* **91,** 246–252 (2002).

2. Roberts, J. A. S. & Bullock, R. M. Direct Determination of Equilibrium Potentials for Hydrogen Oxidation/Production by Open Circuit Potential Measurements in Acetonitrile. *Inorg. Chem.* **52,** 3823–3835 (2013).

3. Karunadasa, H. I., Chang, C. J. & Long, J. R. A molecular molybdenum-oxo catalyst for generating hydrogen from water. *Nature* **464,** 1329–1333 (2010).

4. Costentin, C., Drouet, S., Robert, M. & Savéant, J.-M. Turnover Numbers, Turnover Frequencies, and Overpotential in Molecular Catalysis of Electrochemical Reactions. Cyclic Voltammetry and Preparative-Scale Electrolysis. *J. Am. Chem. Soc.* **134,** 11235–11242 (2012).

5. Rountree, E. S., McCarthy, B. D., Eisenhart, T. T. & Dempsey, J. L. Evaluation of Homogeneous Electrocatalysts by Cyclic Voltammetry. *Inorg. Chem.* **53,** 9983–10002 (2014).